Superconductivity in epitaxial PtSb(0001) thin films

C. Müller,[1,2,*] S. P. Bommanaboyena,[1] A. Badura,[1,2] T. Uchimura,[3] F. Husstedt,[4,5] B. V. Schwarze,[4] S. Banerjee,[1,6] M. Ledinský,[1] J. Michalicka,[1,7] M. Míšek,[1] P. Proschek,[2] M. Šindler,[1] C. Timm,[8,9] T. Helm,[4] S. Fukami,[3] F. Krizek,[1,10] and D. Kriegner[1,†]

[1]*Institute of Physics, Czech Academy of Sciences, 162 00 Prague, Czech Republic*
[2]*Faculty of Mathematics and Physics, Charles University, 121 16 Prague, Czech Republic*
[3]*Research Institute of Electrical Communication, Tohoku University, Sendai 980-8577, Japan*
[4]*Hochfeld-Magnetlabor Dresden (HLD-EMFL), Helmholtz-Zentrum Dresden-Rossendorf, 01328 Dresden, Germany*
[5]*Institute of Solid State and Materials Physics, Technische Universität Dresden, 01062 Dresden, Germany*
[6]*Faculty of Nuclear Sciences and Physical Engineering, Czech Technical University in Prague, 120 00 Prague, Czech Republic*
[7]*Central European Institute of Technology, Brno University of Technology, 612 00 Brno, Czech Republic*
[8]*Würzburg-Dresden Cluster of Excellence ctd.qmat, 01069 Dresden, Germany*
[9]*Institute of Theoretical Physics, Technische Universität Dresden, 01062 Dresden, Germany*
[10]*Faculty of Nuclear Sciences and Physical Engineering, Czech Technical University in Prague, 11519 Prague, Czech Republic*

(Received 13 May 2026; accepted 11 August 2026; published 4 September 2026)

Building on earlier reports of superconductivity in bulk PtSb, we present a systematic study of superconductivity in epitaxial PtSb(0001) thin films grown on $SrF_2(111)$. Electrical transport measurements reveal a superconducting transition at $T_c = 1.72$ K. The field-induced broadening of the transition and the temperature dependence of the upper critical fields are consistent with type-II superconductivity. We determine the upper critical fields for magnetic fields applied perpendicular and parallel to the film plane and parametrize their temperature dependence using an anisotropic Ginzburg-Landau approach. For a representative film in the intermediate thickness regime ($d = 50$ nm), we obtain coherence lengths of $\xi_{ab} \approx 56$ nm and $\xi_c \approx 14$ nm. Current-voltage characteristics show sizable critical currents, with a critical current density reaching $J_c \approx 6 \times 10^4$ A/cm^2 at 0.5 K. These results establish the superconducting properties of epitaxial PtSb thin films and provide a basis for lattice-matched heterostructures within the NiAs-type materials family.

DOI: 10.1103/zjt7-88m9

I. INTRODUCTION

Epitaxial superconducting thin films underpin both quantum and cryogenic electronics and controlled proximity heterostructures, where interfacial quality, crystallographic registry, and symmetry matching are often decisive [1,2]. Compared with polycrystalline layers, single-crystalline films enable reproducible nanofabrication, well-defined anisotropy studies, and systematic interface engineering in superconductor/metal and superconductor/magnet heterostructures. Such proximity-coupled superconducting heterostructures constitute a central route toward superconducting spintronics and related device concepts [3–6]. The NiAs-type structure (space group $P6_3/mmc$, No. 194) offers an especially versatile platform in this regard: it hosts multiple superconductors alongside a wide range of magnetic compounds with closely matched lattice parameters, enabling epitaxial heterostructures [7,8].

Among the superconducting members of this family, PtSb is particularly compelling yet comparatively unexplored. Superconductivity in bulk PtSb was first reported by Matthias *et al.*, with $T_c \approx 2.1$ K [9], and bulk superconductivity has since been found in several other $P6_3/mmc$ intermetallics, including PdSb, PdTe, NiBi, PtBi, PtSn, and RhBi [10–15]. More recently, Hirai *et al.* [16] studied the high-entropy antimonide series $(RuRhPdIr)_{1-x}Pt_xSb$ and reported composition- and disorder-tunable superconductivity, including an enhanced H_{c2} in the strongly disordered regime; the polycrystalline PtSb end member of that series is consistent with the earlier report.

The same structure family also hosts magnetic compounds, including the ferromagnets MnAs, MnBi, MnSb, and CrTe [17–19], and the collinear compensated magnetically ordered members MnTe and CrSb, recently identified as altermagnets [20–27]. Notably, CrSb is closely lattice matched to PtSb, and PtSb/CrSb heterostructures exploiting their common NiAs-type structure have already been realized [8]. Epitaxial growth has been also demonstrated for MnAs and MnTe [28,29], as well as multiple epitaxial orientations of CrSb [26,30].

In the context of superconducting spintronics, superconductor/ferromagnet proximity effects and Josephson physics are well established, encompassing phenomena such as 0-π transitions and long-range triplet supercurrents [3–6]. More recently, theory has extended these ideas to compensated

*Contact author: mullerch@fzu.cz
†Contact author: kriegner@fzu.cz

Published by the American Physical Society under the terms of the Creative Commons Attribution 4.0 International license. Further distribution of this work must maintain attribution to the author(s) and the published article's title, journal citation, and DOI.

magnets: superconductor/altermagnet hybrids are predicted to host a range of distinctive proximity and Josephson phenomena [31–48]. Realizing such phenomena experimentally, across both the ferromagnetic and altermagnetic members of the NiAs-type family, first requires establishing high-quality epitaxial superconducting thin films within this materials system.

Here, we report superconductivity in single-crystalline epitaxial PtSb(0001) thin films grown on $SrF_2(111)$. While superconductivity is well established in polycrystalline bulk PtSb, its realization and properties in epitaxial thin-film form have, to our knowledge, not previously been reported. Combining structural characterization with electrical transport measurements across a film-thickness series from 15 nm to 100 nm, we determine the superconducting transition temperature, quantify the anisotropic upper critical fields and coherence lengths within a Ginzburg-Landau framework, and measure the critical current densities. These results demonstrate epitaxial PtSb as a robust single-crystalline superconducting platform and lay the groundwork for lattice-matched proximity heterostructures, including superconductor/altermagnet junctions, across the wider NiAs-type materials family.

II. EXPERIMENTAL METHODS

Epitaxial PtSb(0001) thin films were grown by dc magnetron cosputtering from elemental Pt and Sb targets (99.99% purity) in a confocal sputtering system. The chamber base pressure was below 3×10^{-8} mbar and sputtering was performed in high-purity Ar (99.999%) at a working pressure of 6.5×10^{-3} mbar. The individual sputter fluxes were monitored by an *in situ* quartz crystal microbalance and adjusted to obtain stoichiometric PtSb. $SrF_2(111)$ substrates (Crystec GmbH) were chosen because they are chemically inert and electrically insulating, and because their hexagonal in-plane surface lattice constant ($a_{\parallel} = a_{SrF_2}/\sqrt{2}$) provides a close lattice match to PtSb(0001). The substrates were held at 400 °C during deposition. Further details about the growth can be found in Ref. [8].

Crystallographic phase purity and out-of-plane orientation were characterized by x-ray diffraction (XRD) symmetric radial scans. Surface morphology was examined by tapping-mode atomic force microscopy (AFM). Cross-sectional microstructure and interface quality were investigated by high-angle annular dark-field imaging with a probe-corrected scanning transmission electron microscope (HAADF-STEM) on focused ion beam (FIB)-prepared lamellae.

For transport measurements, the films were patterned into Hall-bar devices by optical lithography followed by Ar^+ ion milling and measured in a four-probe configuration, with typical channel widths $w \sim 8$–$18\,\mu$m and voltage-probe separations $L \sim 40$–$360\,\mu$m; film thicknesses were in the range $d = 15$ nm–100 nm. The superconducting transition temperature and upper critical fields were determined from resistance measurements as a function of temperature and magnetic field for field orientations perpendicular and parallel to the film plane. Measurements above ~0.5 K were performed in a Quantum Design PPMS with a ^{3}He insert, while lower-temperature data were acquired in a dilution refrigerator using low-frequency lock-in techniques. The differential resistance dV/dI was obtained by numerically differentiating the measured $V(I)$ characteristics as a function of dc bias current and used to determine the critical current density.

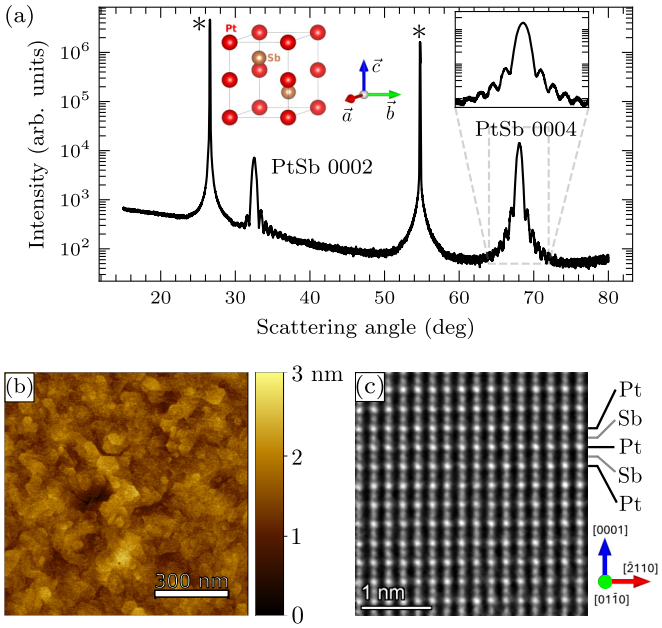


FIG. 1. Structural characterization of epitaxial PtSb(0001) thin films on $SrF_2(111)$. (a) Symmetric XRD radial scan of a 15 nm PtSb(0001) film showing only PtSb 000ℓ reflections together with the substrate peaks marked by a star; Laue thickness fringes indicate uniform thickness and high crystalline coherence. An inset shows the unit cell structure of PtSb [49]. (b) Tapping-mode AFM topography of a 30 nm PtSb(0001) film, revealing ~10–100 nm terraces separated by biatomic steps. (c) Cross-sectional HAADF-STEM image along the $[01\bar{1}0]$ zone axis, resolving the layered stacking of Pt and Sb atomic planes.

III. RESULTS

A. Epitaxy and structural characterization

Figure 1 summarizes the structural characterization of epitaxial PtSb(0001) thin films grown on $SrF_2(111)$. PtSb crystallizes in the hexagonal NiAs-type structure with reported bulk lattice parameters $a = 4.13$ Å and $c = 5.48$ Å [50,51]. The symmetric x-ray diffraction (XRD) radial scan in Fig. 1(a) shows only PtSb 000ℓ Bragg reflections together with the substrate peaks, confirming phase purity and the (0001) growth plane orientation. Pronounced Laue thickness fringes around the PtSb peaks further indicate a uniform thickness and high crystalline coherence. From the out-of-plane peak positions we extract a c-axis lattice parameter of $c = 5.50$ Å, in good agreement with literature [50,51]. The in-plane lattice parameter was determined independently from reciprocal space maps (not shown) and is found to be $a = 4.12$ Å. This corresponds to an in-plane lattice mismatch of order <1% relative to the surface lattice constant of SrF_2 (111), consistent with epitaxial growth. The surface morphology, characterized by tapping-mode atomic force microscopy (AFM) [Fig. 1(b)], exhibits extended terraces with lateral sizes on the order of 10–100 nm separated by biatomic steps,

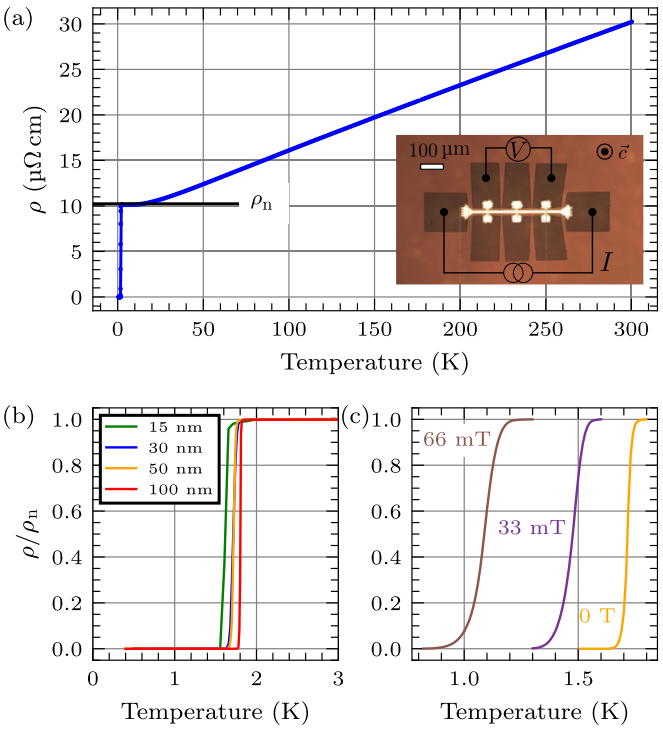


FIG. 2. Superconducting transition in PtSb thin films. (a) Resistivity $\rho(T)$ at zero magnetic field for a 30 nm thick PtSb epitaxial film. An inset shows an optical microscope image of the used device structure. (b) Superconducting transitions in the normalized resistivity for films with thicknesses of 15 nm, 30 nm, 50 nm, and 100 nm (the 30 nm and 50 nm traces largely overlap). (c) Normalized resistivity $\rho(T)/\rho_n$ of a 50 nm film at various magnetic fields applied perpendicular to the film plane, where ρ_n denotes the normal-state resistivity (see main text).

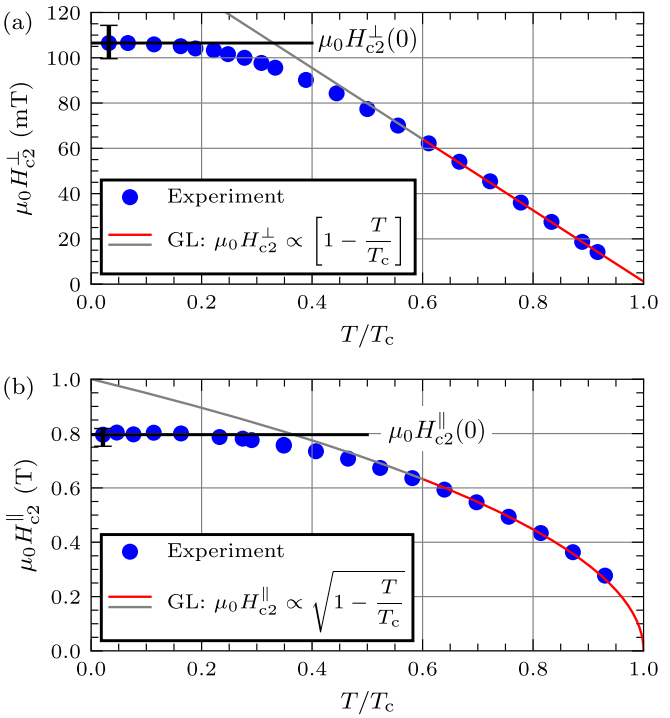


FIG. 3. Upper critical fields for magnetic fields applied perpendicular and parallel to the film plane. (a) Perpendicular upper critical field $\mu_0 H_{c2}^{\perp}$ versus temperature measured in a 50 nm thick PtSb epitaxial film; the solid red line is a fit using Eq. (1). (b) Parallel upper critical field $\mu_0 H_{c2}^{\parallel}$ versus temperature measured in a 30 nm thick film; the solid red line is a fit using Eq. (2). Error bars of $\mu_0 H_{c2}(0)$ are obtained from the analysis in Appendix A.

consistent with step-flow growth on a hexagonal lattice. The root-mean-square surface roughness is 3 Å, in good agreement with the value obtained from x-ray reflectivity (XRR, not shown), and the peak-to-valley height variation amounts to ≈2.5 nm. Finally, the HAADF-STEM image in Fig. 1(c), taken along the [01$\bar{1}$0] zone axis, resolves the layered stacking of alternating Pt- and Sb-containing atomic planes, corroborating the single-crystalline nature of the films and a sharp film/substrate interface. Together, these measurements establish epitaxial PtSb(0001) thin films with high structural quality as a basis for the superconducting transport experiments discussed in the following.

B. Superconducting transition

Figure 2(a) shows the temperature dependence of the resistivity $\rho(T)$ of a representative PtSb device at zero applied magnetic field. In the normal state, the resistivity at $T = 2$ K is $\rho_n = 10.1\,\mu\Omega\,\text{cm}$, corresponding to a residual resistivity ratio RRR $= \rho(300\,\text{K})/\rho(2\,\text{K}) \approx 3$. We define the superconducting transition temperature T_c as the temperature where $\rho(T)$ drops to 50% of ρ_n, yielding $T_c = 1.72$ K for the device shown. For other thicknesses and other extraction criteria, see Appendix A. The transition width ΔT_c, defined as the temperature interval between $0.9\rho_n$ and $0.1\rho_n$, is $\Delta T_c = 0.05$ K. This transition width, which corresponds to a measure of the uncertainty of the transition temperature, slightly varies with thickness from $\Delta T_c = 0.02$ K for 100 nm to $\Delta T_c = 0.08$ K for 15 nm thick PtSb.

Figure 2(b) compares the superconducting transitions for films with thicknesses $d = 15$ nm, 30 nm, 50 nm, and 100 nm. The transitions of the 30 nm and 50 nm films largely overlap, while the 15 nm film exhibits a slightly reduced T_c. In contrast, the 100 nm film shows a slightly enhanced T_c. Such small variations may reflect modest changes in disorder, strain, or finite-size effects between films [52,53], and will not be further analyzed here.

To examine the response to magnetic field, Fig. 2(c) shows the normalized resistivity $\rho(T)/\rho_n$ of a 50 nm film in magnetic fields applied perpendicular to the film plane. With increasing field, the transition shifts to lower temperature and broadens systematically, as commonly observed in thin-film superconductors [54–56]; a more detailed discussion of the field-induced broadening is deferred to the discussion of the critical-field data below.

C. Upper critical fields and coherence lengths

To quantify the superconducting anisotropy, we determined the upper critical field H_{c2} from resistance measurements with magnetic field applied perpendicular ($\perp$) and parallel ($\parallel$) to the film plane, respectively. The temperature dependences $\mu_0 H_{c2}^{\perp}(T)$ and $\mu_0 H_{c2}^{\parallel}(T)$ are summarized in Fig. 3. The critical fields were extracted from magnetic-field sweeps

TABLE I. Critical temperature, upper critical fields, coherence lengths, and anisotropy parameter $\gamma = \mu_0 H_{c2}^{\parallel}/\mu_0 H_{c2}^{\perp} = \xi_{ab}/\xi_c$ [57,58] for different film thicknesses. The perpendicular and parallel upper critical fields, $\mu_0 H_{c2}^{\perp}$ and $\mu_0 H_{c2}^{\parallel}$, were determined from the experimentally measured critical fields at the lowest accessible temperature. The in-plane coherence length ξ_{ab} and the out-of-plane coherence length ξ_c were subsequently calculated using Eq. (1) and Eq. (3), respectively. Relative uncertainties for the listed quantities are typically smaller than 5% for T_c, 10% for H_{c2}, 3% and 10% for ξ_{ab} and ξ_c, and 15% for γ.

d (nm)	T_c (K)	$\mu_0 H_{c2}^{\perp}$ (mT)	ξ_{ab} (nm)	$\mu_0 H_{c2}^{\parallel}$ (mT)	ξ_c (nm)	γ
15	1.62	110	54.6	2169	2.8	19.7
30	1.71	73	67.1	796	6.2	10.9
50	1.72	107	55.5	425	14	4
100	1.8	104	56.3	210	27.9	2

using a resistive criterion of $0.9\rho_n$, where ρ_n denotes the normal-state resistivity. For each temperature, the reported values correspond to the mean of the absolute critical fields obtained from forward and backward sweeps in both field polarities.

To parametrize the data, we employ standard Ginzburg-Landau expressions for anisotropic and thin-film superconductors [57–60]. For $\mu_0 H$ perpendicular to the film plane, the temperature dependence of the upper critical field is given by

$$\mu_0 H_{c2}^{\perp}(T) = \frac{\Phi_0}{2\pi \xi_{ab}^2}\left[1 - \frac{T}{T_c}\right], \tag{1}$$

where $\Phi_0 = h/2e$ is the magnetic flux quantum and ξ_{ab} denotes the in-plane coherence length at low temperatures. For $\mu_0 H$ parallel to the film plane and sufficiently close to T_c, we use the thin-film expression introduced by Tinkham [57,58],

$$\mu_0 H_{c2}^{\parallel}(T) = \frac{\sqrt{3}\Phi_0}{\pi d \xi_{ab}}\sqrt{1 - \frac{T}{T_c}}. \tag{2}$$

This expression applies when the film thickness d is smaller than the temperature-dependent out-of-plane coherence length $\xi_c(T)$ such that orbital pair breaking for an in-plane magnetic field is governed by the finite film thickness. Since $\xi_c(T) \propto [1 - T/T_c]^{-1/2}$ decreases upon cooling it eventually becomes smaller than d, and a crossover toward the three-dimensional anisotropic expression is expected [57]:

$$\mu_0 H_{c2}^{\parallel}(0) = \frac{\Phi_0}{2\pi \xi_{ab}\xi_c}. \tag{3}$$

The zero-temperature in-plane coherence length ξ_{ab} is calculated from the measured perpendicular upper critical field according to

$$\xi_{ab} = \sqrt{\frac{\Phi_0}{2\pi \mu_0 H_{c2}^{\perp}(0)}}, \tag{4}$$

as obtained from Eq. (1).

The resulting critical fields and coherence lengths, taken from the lowest measured temperature for different film thicknesses, are summarized in Table I. Uncertainties of the derived quantities are obtained from the dependence of H_{c2} on the criterion used for its determination (see Appendix A).

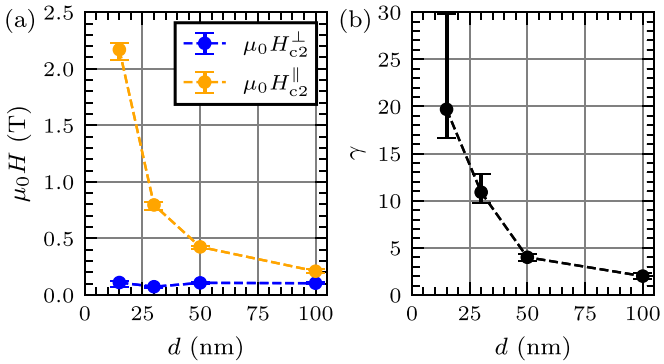


FIG. 4. Visualization of Table I. (a) Upper critical fields $\mu_0 H_{c2}^{\perp}$ and $\mu_0 H_{c2}^{\parallel}$ near 0 K for all measured thicknesses. (b) Thickness dependence of the anisotropy parameter γ.

As shown in Fig. 3(a), $\mu_0 H_{c2}^{\perp}(T)$ is well described by Eq. (1) in the temperature range $T/T_c \gtrsim 0.6$. The fit was performed over the temperature range $0.6 \leqslant T/T_c \leqslant 1$, chosen to remain within the regime where Ginzburg–Landau theory is expected to be applicable while retaining a sufficient number of data points for a reliable fit. In order to describe the full temperature range, we use the Werthamer-Helfand-Hohenberg model, as applied in Appendix B. For $\mu_0 H$ parallel to the film plane [Fig. 3(b)], $\mu_0 H_{c2}^{\parallel}(T)$ follows the expected trend near T_c of Eq. (2), consistent with the behavior discussed for thin-film superconductors by Drew *et al.* [61]. Overall, the field-orientation dependence and variation of H_{c2} are consistent with anisotropic type-II superconductivity in PtSb, in line with magnetization data reported for related antimonides including the PtSb end member [16]. Using the values in Table I, the film thicknesses satisfy $d \gtrsim \xi_c$ for $T \to 0$ K for all samples, indicating that the films are not in the strict two-dimensional limit, justifying the use of Eq. (3). Additionally, we confirmed that not only the structural film thickness but also the effective superconducting layer thickness exceeds the low temperature coherence length (see Appendix C for details). Within anisotropic Ginzburg-Landau theory, the superconducting anisotropy can be expressed as $\gamma = \mu_0 H_{c2}^{\parallel}/\mu_0 H_{c2}^{\perp} = \xi_{ab}/\xi_c$ [57,58]. The resulting γ values, listed in Table I, decrease systematically with increasing film thickness, consistent with the explicit thickness dependence of $H_{c2}^{\parallel}$ given by Eq. (2). The extracted γ should therefore be regarded as an effective anisotropy influenced by the reduced dimensionality and thin-film geometry, rather than a direct measure of the intrinsic superconducting anisotropy of PtSb. Since superconducting PtSb has not really been realized in sufficiently thick epitaxial films, the intrinsic bulk anisotropy cannot be determined from the present data. We note that, owing to the sharp resistive transition, varying the resistive criterion within reasonable bounds has only a minor influence on the extracted values. The upper critical fields $\mu_0 H_{c2}^{\perp}$ and $\mu_0 H_{c2}^{\parallel}$ listed in Table I are shown in Fig. 4(a), while γ is shown in Fig. 4(b).

D. Critical current density

Figure 5 summarizes the current-driven transport of PtSb in the superconducting state. Current-voltage characteristics

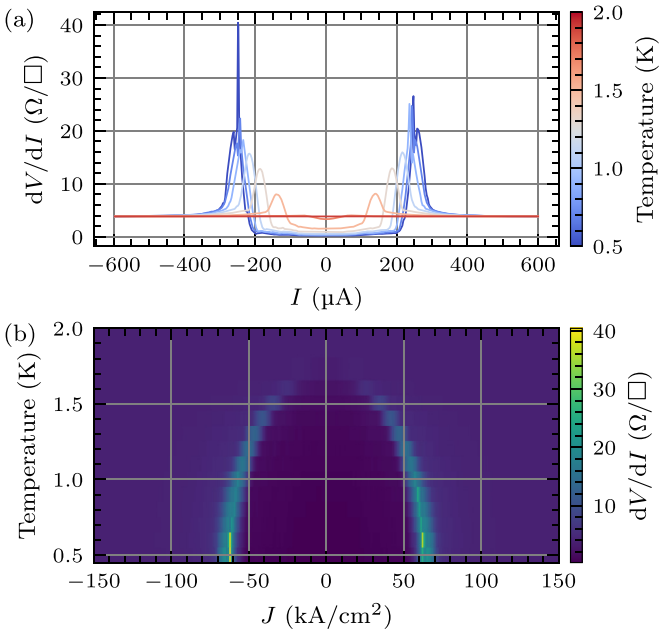


FIG. 5. Current-driven transport in PtSb. (a) Differential resistance dV/dI, obtained by numerical differentiation of measured $V(I)$ characteristics, shown as a function of current for a 50 nm thick PtSb film at temperatures from 0.5 K to 1.9 K in 0.2 K steps. Here dV/dI is converted to a differential sheet resistance (in $\Omega/\square$) to normalize out the Hall-bar geometry. (b) Color map of dV/dI as a function of current density J and temperature. The critical current density J_c is extracted from the position of the maximum in dV/dI (see text) and reaches $62.2 \pm 1.2\,\mathrm{kA/cm^2}$ at 0.5 K.

$V(I)$ were recorded at fixed temperature, and the differential resistance dV/dI shown in Fig. 5 was obtained by numerical differentiation. Figure 5(a) displays $dV/dI(I)$ for a 50 nm thick film measured at temperatures from 0.5 K to 1.9 K. At low temperatures, dV/dI exhibits a sharp peak at a characteristic bias current, which shifts to lower current and broadens upon increasing temperature, consistent with a progressive suppression of superconductivity.

We define the critical current I_c as the current at which dV/dI reaches its maximum, corresponding to the steepest point of the measured $V(I)$ characteristic for a given temperature. The critical current density is then obtained as $J_c = I_c/(wd)$, where w and d are the width of the device and the thickness of the film, respectively. The resulting evolution of dV/dI as a function of current density J and temperature is summarized in the color map in Fig. 5(b). Using this definition, we obtain a critical current density of $J_c \approx 60\,\mathrm{kA/cm^2}$ at $T = 0.5\,\mathrm{K}$ for the 50 nm film. All $R(T)$ and $R(H)$ measurements discussed above were performed at substantially smaller excitation current densities (typically $\sim 2.5\,\mathrm{kA/cm^2}$), ensuring that the extracted transition temperatures and upper critical fields are not affected by bias-current-induced suppression.

IV. DISCUSSION AND OUTLOOK

The data in Figs. 1–5 establish epitaxial PtSb(0001) thin films on $SrF_2(111)$ as a reproducible superconducting thin-film platform. Structural characterization (Fig. 1) evidences single-crystalline growth with low surface roughness and lattice parameters close to bulk values, providing a well-defined basis for transport experiments. The resistive transitions (Fig. 2) are sharp and consistent across multiple thicknesses, with only modest variations of T_c in different film thicknesses. Such small variations are common in superconducting thin films and can reflect subtle differences in disorder, strain, or finite-size effects [52,53]. It is conceivable that such factors also contribute to the differences in T_c observed between our epitaxial films and previously reported bulk values. The field-broadened resistive transitions under a perpendicular magnetic field [Fig. 2(c)] are commonly found in superconductors where thermally activated vortex motion contributes to finite resistance below the upper critical field [54–56]. This behavior is consistent with type-II superconductivity in PtSb. In support of this classification, magnetization data reported for the related antimonide series $(RuRhPdIr)_{1-x}Pt_xSb$, including the PtSb end member, show the characteristic behavior expected for a type-II superconductor [16]. While we do not pursue a detailed analysis of the transition broadening here, the systematic shift and broadening with field are consistent with the overall picture of anisotropic superconductivity in these films.

Upper critical fields measured for out-of-plane and in-plane field orientations (Fig. 3) reveal pronounced anisotropy that decreases with increasing thickness. Parametrizing the data with anisotropic Ginzburg-Landau relations yields in-plane and out-of-plane coherence lengths summarized in Table I and visualized in Fig. 4. Both $\mu_0 H_{c2}^{\perp}$ and $\mu_0 H_{c2}^{\parallel}$ follow the expected temperature trend close to T_c predicted from the Ginzburg-Landau theory, but exhibit a weaker temperature dependence at low temperatures. Similar low-temperature deviations from simple near-T_c parametrizations have been discussed in other thin-film superconductors [59,60,62,63]. Generally the measured maximal critical magnetic field values are well below the weak-coupling Pauli paramagnetic limit $\mu_0 H_P \approx 1.84\,T_c$ [64,65], which for $T_c = 1.72\,\mathrm{K}$ yields $\mu_0 H_P \approx 3.2\,\mathrm{T}$. This suggests that orbital pair breaking provides the dominant limitation in PtSb. This is consistent with the results of the Werthamer-Helfand-Hohenberg theory (Appendix B) as well as previous analysis in Ref. [16]. Importantly, the resulting coherence lengths satisfy $d \gtrsim \xi_c$ for all samples, indicating that the films are not in the strict two-dimensional limit.

Placing the extracted parameters into the broader context of NiAs-type superconductors, the in-plane coherence length of the thickest PtSb film ($\xi_{ab} \approx 56\,\mathrm{nm}$) is comparable to the values reported for bulk PdSb ($\xi_{ab} \approx 61\,\mathrm{nm}$) [15] and bulk PdTe ($\xi_{ab} \approx 48\,\mathrm{nm}$) [14]. Likewise, the superconducting transition temperatures of these NiAs-type intermetallics fall in a similar range [9–11]. Together, this comparison supports that epitaxial PtSb thin films realize superconductivity with characteristic length scales typical for this structure family, while offering the key advantage of compatibility with lattice-matched epitaxial heterostructures.

At 0.5 K, we obtain a critical current density of $J_c \approx 6 \times 10^4\,\mathrm{A/cm^2}$ [Fig. 5]. Since, to the best of our knowledge, systematic studies of J_c in NiAs-type superconductors are lacking, we place this value in the broader context of

established superconducting thin-film platforms. The measured J_c is below the values of up to $\sim 10^6$–10^7, A/cm^2 reported for optimized Nb-, NbN-, and Al-based thin-film structures [66,67]. In sufficiently narrow structures, vortex entry and motion can be suppressed, allowing the critical current to approach the Ginzburg-Landau depairing limit. By contrast, our measurements were performed on micrometer-wide strips with $w \gg \xi$, for which lower critical current densities are generally expected. The present value therefore provides a representative measure of the current-carrying capability of epitaxial PtSb devices in this geometry. Together with the anisotropic H_{c2} behavior and the structural quality, this establishes epitaxial PtSb(0001) as a reproducible superconducting thin-film material within the NiAs-type family. Our results quantify the key transport characteristics—transition temperature, anisotropic coherence lengths, and critical current densities—positioning PtSb as a promising platform for superconducting electronics and proximity heterostructures. In particular, the compatibility with other NiAs-type compounds motivates future studies of lattice-matched stacks involving recently identified altermagnets, where PtSb could serve as a well-defined superconducting building block.

ACKNOWLEDGMENTS

We acknowledge financial support by the Czech Science Foundation (Grant No. 22-22000M); Lumina Quaeruntur fellowships LQ100102201 and LQ100102602 of the Czech Academy of Sciences; Czech Ministry of Education, Youth and Sports (MEYS) Grants No. CZ.02.01.01/00/22_-008/0004594, No. LM2023065, and No. LM2023051; INTER-COST Project No. LUC24098, and ERC Advanced Grant No. 101095925; Deutsche Forschungsgemeinschaft (DFG, German Research Foundation) through SFB 1143 (Project ID 247310070, Projects A04 and C01), as well as HE 8556/3-1 and the Würzburg-Dresden Cluster of Excellence ctd.qmat (EXC 2147, Project ID 390858490). We are grateful to Zbyněk Šobáň from the Institute of Physics, Czech Academy of Sciences, for technical support and assistance. Experiments were partly performed in MGML (mgml.eu), and CzechNanoLab Research Infrastructure.

DATA AVAILABILITY

The numerical data presented in the figures of this manuscript are available in a Zenodo repository [68].

APPENDIX A: CRITERION DEPENDENCE

To evaluate the criterion dependence of the extracted transition, temperature T_c (Fig. 6) and the upper critical fields H_{c2} (Fig. 7) were determined using the $0.1\rho_n$, $0.5\rho_n$, and $0.9\rho_n$ resistance criteria. As expected, the absolute values depend slightly on the chosen criterion, while the overall dependence remains unchanged.

APPENDIX B: WERTHAMER-HELFAND-HOHENBERG MODELING

In addition to the phenomenological Ginzburg-Landau (GL) analysis presented in the main text, the temperature dependence of the out-of-plane upper critical field was analyzed within the framework of the Werthamer-Helfand-Hohenberg (WHH) theory [69]. The WHH model is characterized by four parameters: (i) the superconducting transition temperature T_c, (ii) the electron diffusion coefficient, which determines the initial slope of $H_{c2}(T)$ close to T_c, (iii) the Maki parameter α, which quantifies the relative importance of Pauli paramagnetic pair breaking with respect to orbital pair breaking, and (iv) the spin-orbit scattering parameter.

Figure 8 compares the experimental data with the corresponding WHH calculations. First, only the transition temperature T_c and the diffusion coefficient were treated as free parameters while fixing the Maki and spin-orbit scattering parameters to zero. As shown by the red curve, this purely

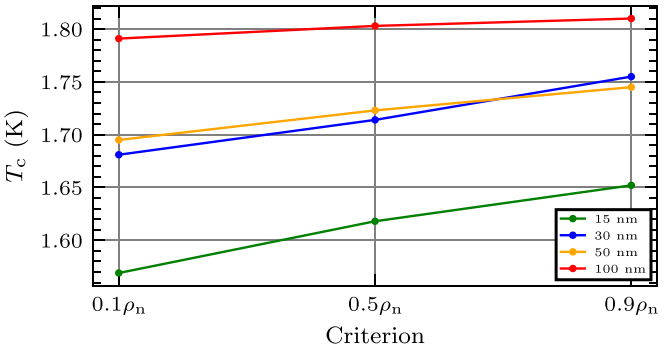


FIG. 6. Extracted superconducting transition temperature T_c as a function of the resistance criterion given as a fraction of the normal resistivity ρ_n determined at $T = 2$ K.

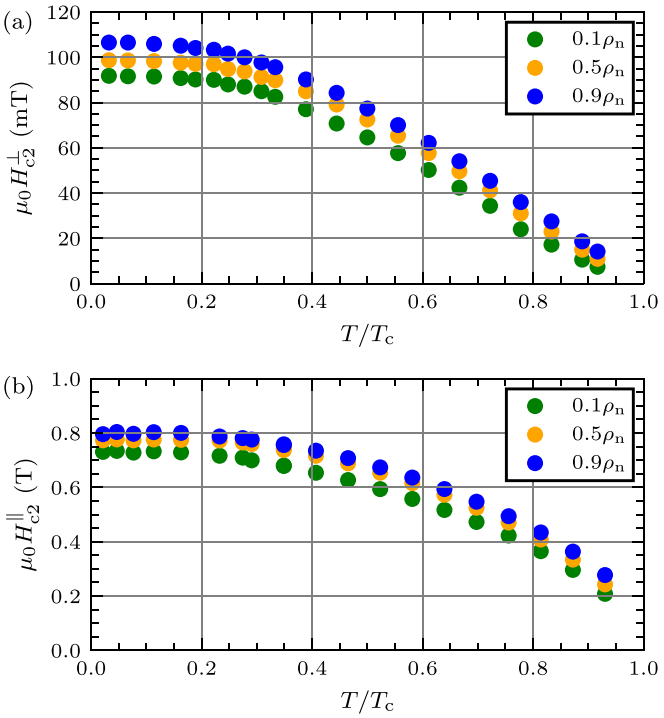


FIG. 7. Extracted upper critical fields H_{c2} as a function of the temperature for different resistance criteria.

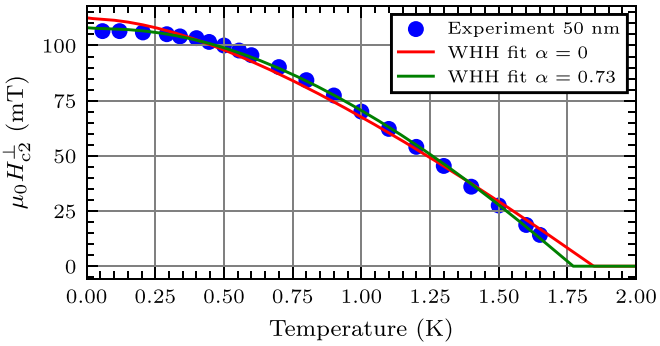


FIG. 8. Upper critical field $\mu_0 H_{c2}^{\perp}$ of a 50 nm thick PtSb epitaxial film as a function of temperature. The solid lines represent WHH model fits with $\alpha = 0$ fixed (red) and with α as a free fitting parameter (green).

orbital model captures the overall behavior but does not fully reproduce the measured temperature dependence. Allowing for a finite Maki parameter while simultaneously fitting T_c, and the diffusion coefficient results in an improved agreement with the experimental data over the entire temperature range (green curve), yielding a best-fit value of $\alpha = 0.73$. Within the WHH framework, this value suggests that orbital pair breaking remains the dominant mechanism limiting the upper critical field, while Pauli paramagnetic effects may provide an additional contribution. Allowing the spin-orbit scattering parameter to vary did not lead to a further noticeable improvement of the fit quality.

Overall, the characteristic zero-temperature upper critical field obtained from the WHH analysis is consistent with the value extracted from the GL analysis presented in the main text. While both approaches yield comparable values for $\mu_0 H_{c2}^{\perp}(0)$, the WHH model provides a more accurate description of the complete temperature dependence of the experimental data.

TABLE II. Comparison of the nominal structural film thickness d and the effective thickness d_{eff} obtained from Eq. (C1).

d (nm)	d_{eff} (nm)
15	9.8 ± 0.3
30	21.8 ± 0.2
50	46.7 ± 1.5
100	94.5 ± 1.3

APPENDIX C: EFFECTIVE-THICKNESS ANALYSIS

To validate the use of the structural film thickness in the analysis of the in-plane upper critical field, we performed an independent consistency check using the following procedure. First, the in-plane coherence length $\xi_{ab}(0\,\text{K})$ was extracted from the out-of-plane upper critical field using the near-T_c Ginzburg-Landau analysis described in Eq. (1) and shown in Fig. 3(a).

The extrapolated zero-temperature coherence length $\xi_{ab}(0\,\text{K})$ was subsequently kept fixed while fitting the near-T_c in-plane upper critical field using

$$\mu_0 H_{c2}^{\parallel}(T) = \frac{\sqrt{3}\Phi_0}{\pi d_{\text{eff}} \xi_{ab}} \sqrt{1 - \frac{T}{T_c}}, \tag{C1}$$

with the effective superconducting thickness d_{eff} as the only free fitting parameter. The extracted effective superconducting thicknesses are summarized in Table II. The superconducting thicknesses are found to be just 3–8 nm lower compared to the nominal structural film thicknesses, supporting the assumption that the structural thickness provides a reasonable estimate of the superconducting thickness used throughout the manuscript. Furthermore, for all investigated films, the extracted effective thickness exceeds the out-of-plane coherence length ξ_c, confirming that the dimensional crossover discussed in the main text remains valid.

[1] P. Krantz, M. Kjaergaard, F. Yan, T. P. Orlando, S. Gustavsson, and W. D. Oliver, A quantum engineer's guide to superconducting qubits, Appl. Phys. Rev. **6**, 021318 (2019).

[2] M. Kjaergaard, M. E. Schwartz, J. Braumüller, P. Krantz, J. I.-J. Wang, S. Gustavsson, and W. D. Oliver, Superconducting qubits: Current state of play, Annu. Rev. Condens. Matter Phys. **11**, 369 (2020).

[3] A. I. Buzdin, Proximity effects in superconductor-ferromagnet heterostructures, Rev. Mod. Phys. **77**, 935 (2005).

[4] F. S. Bergeret, A. F. Volkov, and K. B. Efetov, Odd triplet superconductivity and related phenomena in superconductor-ferromagnet structures, Rev. Mod. Phys. **77**, 1321 (2005).

[5] M. Eschrig, Spin-polarized supercurrents for spintronics, Phys. Today **64**(1), 43 (2011).

[6] J. Linder and J. W. A. Robinson, Superconducting spintronics, Nat. Phys. **11**, 307 (2015).

[7] C. W. Burrows, J. D. Aldous, and G. R. Bell, Epitaxial growth and surface reconstruction of CrSb(0001), Results Phys. **12**, 1783 (2019).

[8] S. P. Bommanaboyena, C. Müller, M. Jarošová, K. Wolk, S. Telkamp, P. Zeng, F. Krizek, T. Uchimura, A. Badura, K. Olejník, D. Scheffler, K. Beranová, S. Banerjee, M. Ledinský, H. Reichlová, T. Jungwirth, L. Horák, and D. Kriegner, Single-crystalline CrSb(0001) thin films grown by dc magnetron co-sputtering, Phys. Rev. Mater. **9**, 064402 (2025).

[9] B. T. Matthias, Superconducting compounds of nonsuperconducting elements, Phys. Rev. **90**, 487 (1953).

[10] B. T. Matthias, Transition temperatures of superconductors, Phys. Rev. **92**, 874 (1953).

[11] B. T. Matthias, T. H. Geballe, and V. B. Compton, Superconductivity, Rev. Mod. Phys. **35**, 1 (1963).

[12] D. Hamilton, Ch.J. Raub, B. Matthias, E. Corenzwit, and G. Hull, Some new superconducting compounds, J. Phys. Chem. Solids **26**, 665 (1965).

[13] B. W. Roberts, Survey of superconductive materials and critical evaluation of selected properties, J. Phys. Chem. Ref. Data **5**, 581 (1976).

[14] A. B. Karki, D. A. Browne, S. Stadler, J. Li, and R. Jin, PdTe: A strongly coupled superconductor, J. Phys.: Condens. Matter **24**, 055701 (2012).

[15] C. Chen, D. Zhang, R. Kumar, Y. Zhang, G. Ye, L. Yin, J. Zhang, H. Yuan, C. Cao, and X. Lu, Tip-induced superconductivity enhancement in single-crystalline PdSb by point-contact spectroscopy, Phys. Rev. B **106**, 174520 (2022).

[16] D. Hirai, N. Uematsu, Y. Muramatsu, K. Deguchi, Y. Shimura, T. Onimaru, and K. Takenaka, Increased superconducting transition temperature and upper critical field of a high-entropy antimonide superconductor $(RuRhPdIr)_{1-x}Pt_xSb$, Chem. Mater. **36**, 9547 (2024).

[17] W. J. Takei, D. E. Cox, and G. Shirane, Magnetic structures in the MnSb-CrSb system, Phys. Rev. **129**, 2008 (1963).

[18] W. J. Takei, D. E. Cox, and G. Shirane, Magnetic structures in CrTe—CrSb solid solutions, J. Appl. Phys. **37**, 973 (1966).

[19] K. R. A. Ziebeck and K.-U. Neumann, 1.5.5.3.3.4 C1b compounds, in *Alloys and Compounds of d-Elements with Main Group Elements. Part 2*, edited by H. P. J. Wijn, Landolt-Börnstein- Group III Condensed Matter Vol. 32C (Springer-Verlag, Berlin, Heidelberg, 2001).

[20] L. Šmejkal, J. Sinova, and T. Jungwirth, Beyond conventional ferromagnetism and antiferromagnetism: A phase with nonrelativistic spin and crystal rotation symmetry, Phys. Rev. X **12**, 031042 (2022).

[21] L. Šmejkal, J. Sinova, and T. Jungwirth, Emerging research landscape of altermagnetism, Phys. Rev. X **12**, 040501 (2022).

[22] R. D. Gonzalez Betancourt, J. Zubáč, R. Gonzalez-Hernandez, K. Geishendorf, Z. Šobáň, G. Springholz, K. Olejník, L. Šmejkal, J. Sinova, T. Jungwirth, S. T. B. Goennenwein, A. Thomas, H. Reichlová, J. Železný, and D. Kriegner, Spontaneous anomalous Hall effect arising from an unconventional compensated magnetic phase in a semiconductor, Phys. Rev. Lett. **130**, 036702 (2023).

[23] S. Lee, S. Lee, S. Jung, J. Jung, D. Kim, Y. Lee, B. Seok, J. Kim, B. G. Park, L. Šmejkal, C.-J. Kang, and C. Kim, Broken Kramers degeneracy in altermagnetic MnTe, Phys. Rev. Lett. **132**, 036702 (2024).

[24] J. Krempaský, L. Šmejkal, S. W. D'Souza, M. Hajlaoui, G. Springholz, K. Uhlířová, F. Alarab, P. C. Constantinou, V. Strocov, D. Usanov, W. R. Pudelko, R. González-Hernández, A. Birk Hellenes, Z. Jansa, H. Reichlová, Z. Šobáň, R. D. Gonzalez Betancourt, P. Wadley, J. Sinova, D. Kriegner, *et al.*, Altermagnetic lifting of Kramers spin degeneracy, Nature (London) **626**, 517 (2024).

[25] T. Osumi, Observation of a giant band splitting in altermagnetic MnTe, Phys. Rev. B **109**, 115102 (2024).

[26] S. Reimers, L. Odenbreit, L. Šmejkal, V. N. Strocov, P. Constantinou, A. B. Hellenes, R. Jaeschke Ubiergo, W. H. Campos, V. K. Bharadwaj, A. Chakraborty, T. Denneulin, W. Shi, R. E. Dunin-Borkowski, S. Das, M. Kläui, J. Sinova, and M. Jourdan, Direct observation of altermagnetic band splitting in CrSb thin films, Nat. Commun. **15**, 2116 (2024).

[27] Z. Zhou, X. Cheng, M. Hu, R. Chu, H. Bai, L. Han, J. Liu, F. Pan, and C. Song, Manipulation of the altermagnetic order in CrSb via crystal symmetry, Nature (London) **638**, 645 (2025).

[28] M. Tanaka, J. P. Harbison, T. Sands, T. L. Cheeks, V. G. Keramidas, and G. M. Rothberg, Molecular beam epitaxy of MnAs thin films on GaAs, J. Vac. Sci. Technol. B **12**, 1091 (1994).

[29] D. Kriegner, K. Výborný, K. Olejník, H. Reichlová, V. Novák, X. Marti, J. Gazquez, V. Saidl, P. Němec, V. V. Volobuev, G. Springholz, V. Holý, and T. Jungwirth, Multiple-stable anisotropic magnetoresistance memory in antiferromagnetic MnTe, Nat. Commun. **7**, 11623 (2016).

[30] C.-H. Tseng, S. Karube, Y. Shiota, R. Hisatomi, D. Kan, Y. Shimakawa, and T. Ono, Epitaxial growth of altermagnet CrSb via magnetron sputtering, Crystal Growth Design **25**, 9171 (2025).

[31] C. Sun, A. Brataas, and J. Linder, Andreev reflection in altermagnets, Phys. Rev. B **108**, 054511 (2023).

[32] C. W. J. Beenakker and T. Vakhtel, Phase-shifted Andreev levels in an altermagnet Josephson junction, Phys. Rev. B **108**, 075425 (2023).

[33] M. Papaj, Andreev reflection at the altermagnet-superconductor interface, Phys. Rev. B **108**, L060508 (2023).

[34] Z. P. Niu and Z. Yang, Orientation-dependent Andreev reflection in an altermagnet/altermagnet/superconductor junction, J. Phys. D: Appl. Phys. **57**, 395301 (2024).

[35] J. A. Ouassou, A. Brataas, and J. Linder, Dc Josephson effect in altermagnets, Phys. Rev. Lett. **131**, 076003 (2023).

[36] S.-B. Zhang, L.-H. Hu, and T. Neupert, Finite-momentum Cooper pairing in proximitized altermagnets, Nat. Commun. **15**, 1801 (2024).

[37] H. G. Giil and J. Linder, Superconductor-altermagnet memory functionality without stray fields, Phys. Rev. B **109**, 134511 (2024).

[38] S. Banerjee and M. S. Scheurer, Altermagnetic superconducting diode effect, Phys. Rev. B **110**, 024503 (2024).

[39] Q. Cheng, Y. Mao, and Q.-F. Sun, Field-free Josephson diode effect in altermagnet/normal metal/altermagnet junctions, Phys. Rev. B **110**, 014518 (2024).

[40] D. Chakraborty and A. M. Black-Schaffer, Zero-field finite-momentum and field-induced superconductivity in altermagnets, Phys. Rev. B **110**, L060508 (2024).

[41] H. G. Giil, B. Brekke, J. Linder, and A. Brataas, Quasiclassical theory of superconducting spin-splitter effects and spin-filtering via altermagnets, Phys. Rev. B **110**, L140506 (2024).

[42] B. Lu, K. Maeda, H. Ito, K. Yada, and Y. Tanaka, φ Josephson junction induced by altermagnetism, Phys. Rev. Lett. **133**, 226002 (2024).

[43] D. Chakraborty and A. M. Black-Schaffer, Perfect superconducting diode effect in altermagnets, Phys. Rev. Lett. **135**, 026001 (2025).

[44] D. Chakraborty and A. M. Black-Schaffer, Constraints on superconducting pairing in altermagnets, Phys. Rev. B **112**, 014516 (2025).

[45] S. Sumita, M. Naka, and H. Seo, Phase-modulated superconductivity via altermagnetism, Phys. Rev. B **112**, 144510 (2025).

[46] A. Boruah, S. Acharjee, and P. K. Saikia, Field-free Josephson diode effect in an Ising-superconductor/altermagnet/Ising-superconductor Josephson junction, Phys. Rev. B **112**, 054505 (2025).

[47] I. I. Mazin, Notes on altermagnetism and superconductivity, AAPPS Bull. **35**, 18 (2025).

[48] P. Sukhachov, H. G. Giil, B. Brekke, and J. Linder, Coexistence of p-wave magnetism and superconductivity, Phys. Rev. B **111**, L220403 (2025).

[49] K. Momma and F. Izumi, VESTA 3 for three-dimensional visualization of crystal, volumetric and morphology data, J. Appl. Crystallogr. **44**, 1272 (2011).

[50] A. Kjekshus, K. P. Walseth, S. E. Rasmussen, D. Heinegård, A. T. Balaban, and J. C. Craig, On the properties of $Cr_{1+x}Sb$, $Fe_{1+x}Sb$, $Co_{1+x}Sb$, $Ni_{1+x}Sb$, $Pd_{1+x}Sb$, and $Pt_{1+x}Sb$ phases, Acta Chem. Scand. **23**, 2621 (1969).

[51] M. Ellner, On the crystal parameters of some representatives of the NiAs family containing platinum group metals and gold, Z. Kristallogr. Cryst. Mater. **219**, 537 (2004).

[52] T. Schneider and J.-P. Locquet, Dimensional crossover and finite size effects in superconducting films, Physica C **179**, 125 (1991).

[53] J. P. Ruf, H. Paik, N. J. Schreiber, H. P. Nair, L. Miao, J. K. Kawasaki, J. N. Nelson, B. D. Faeth, Y. Lee, B. H. Goodge, B. Pamuk, C. J. Fennie, L. F. Kourkoutis, D. G. Schlom, and K. M. Shen, Strain-stabilized superconductivity, Nat. Commun. **12**, 59 (2021).

[54] V. Marchenko and A. Nikulov, Anisotropy of the resistive transition width of conventional type II superconductors at the second critical field H_{c2}, Physica C **210**, 466 (1993).

[55] C. C. Wang, R. Zeng, X. Xu, and S. X. Dou, Superconducting transition width under magnetic field in MgB_2 polycrystalline samples, J. Appl. Phys. **108**, 093907 (2010).

[56] A. Zeinali, T. Golod, and V. M. Krasnov, Surface superconductivity as the primary cause of broadening of superconducting transition in Nb films at high magnetic fields, Phys. Rev. B **94**, 214506 (2016).

[57] F. E. Harper and M. Tinkham, The mixed state in superconducting thin films, Phys. Rev. **172**, 441 (1968).

[58] M. Tinkham, *Introduction to Superconductivity*, 2nd ed. (Dover Publications, Mineola, New York, 2004).

[59] X. Xing, W. Zhou, J. Wang, Z. Zhu, Y. Zhang, N. Zhou, B. Qian, X. Xu, and Z. Shi, Two-band and Pauli-limiting effects on the upper critical field of 112-type iron pnictide superconductors, Sci. Rep. **7**, 45943 (2017).

[60] P. R. Broussard, Parallel critical field in thin niobium films: Comparison to theory, J. Low Temp. Phys. **189**, 108 (2017).

[61] A. J. Drew, M. W. Wisemayer, D. O. G. Heron, S. Lister, S. L. Lee, A. Potenza, C. H. Marrows, R. M. Dalgliesh, T. R. Charlton, and S. Langridge, Using spin-polarized neutron reflectivity to probe mesoscopic vortex states in a Pb thin-film superconductor, Phys. Rev. B **80**, 134510 (2009).

[62] L. Wang, H. Lim, and C. Ong, Properties of parallel upper critical field within continuous Ginzburg–Landau model, Physica C **383**, 247 (2002).

[63] T. Coffey, C. Martin, C. C. Agosta, T. Kinoshota, and M. Tokumoto, Bulk two-dimensional Pauli-limited superconductor, Phys. Rev. B **82**, 212502 (2010).

[64] A. M. Clogston, Upper limit for the critical field in hard superconductors, Phys. Rev. Lett. **9**, 266 (1962).

[65] B. S. Chandrasekhar, A note on the maximum critical field of high-field superconductors, Appl. Phys. Lett. **1**, 7 (1962).

[66] K. Ilin, D. Henrich, Y. Luck, Y. Liang, M. Siegel, and D. Y. Vodolazov, Critical current of Nb, NbN, and TaN thin-film bridges with and without geometrical nonuniformities in a magnetic field, Phys. Rev. B **89**, 184511 (2014).

[67] T. Morgan-Wall, B. Leith, N. Hartman, A. Rahman, and N. Marković, Measurement of critical currents of superconducting aluminum nanowires in external magnetic fields: Evidence for a Weber blockade, Phys. Rev. Lett. **114**, 077002 (2015).

[68] C. Müller, S. P. Bommanaboyena, A. Badura, T. Uchimura, F. Husstedt, B. V. Schwarze, S. Banerjee, M. Ledinský, J. Michalicka, M. Míšek, P. Proschek, M. Šindler, C. Timm, T. Helm, S. Fukami, F. Krizek, and D. Kriegner, Source data for "Superconductivity in epitaxial PtSb(0001) thin films", Zenodo, 2026, https://doi.org/10.5281/zenodo.20154939.

[69] N. R. Werthamer, E. Helfand, and P. C. Hohenberg, Temperature and purity dependence of the superconducting critical field, H_{c2}. III. Electron spin and spin-orbit effects, Phys. Rev. **147**, 295 (1966).